1 **Characteristic of atmospheric mercury in a suburban area of East China: sources,**

2 **formation mechanisms, and regional transport**

3 Xiaofei Qin[1], Xiaohao Wang[2], Yijie Shi[1], Guangyuan Yu[1], Na Zhao[1], Yanfen Lin[2], Qingyan Fu[2],

4 Dongfang Wang[2], Zhouqing Xie[3], Congrui Deng[1,*], Kan Huang[1,*]

5 [1]*Center for Atmospheric Chemistry Study, Shanghai Key Laboratory of Atmospheric Particle*

6 *Pollution and Prevention (LAP³), Department of Environmental Science and Engineering, Fudan*

7 *University, Shanghai, 200433 China*

8 [2]*Shanghai Environmental Monitoring Center, Shanghai, 200030 China*

9 [3]*School of Earth and Space Sciences, University of Science and Technology of China, Hefei, Anhui,*

10 *230026 China*

11

12 Correspondence: huangkan@fudan.edu.cn, congruideng@fudan.edu.cn

13

14 **Abstract**

15 Speciated atmospheric mercury including gaseous elemental mercury (GEM), gaseous oxidized

16 mercury (GOM), and particulate-bound mercury (PBM) were measured continuously for one year

17 period at a suburban site, representing a regional transport intersection zone, in East China. Annual

18 mean concentrations of GEM, PBM, and GOM reached 2.77 ng/m³, 60.8 pg/m³, and 82.1 pg/m³,

19 respectively. GEM concentrations were elevated in all the seasons except autumn. High mercury

20 concentrations were related to winds from the south, southwest, and north of the measurement site.

21 Combining analysis results from using various source apportionment methods, it was found that

22 GEM concentration was higher when quasi-local sources dominated over long-range transport. Six

23 source factors belonging to the anthropogenic sources of GEM were identified, including the

24 common sectors previously identified (industrial and biomass burning, coal combustion, iron and

25 steel production, cement production, and incineration), as well as an additional factor of shipping

26 emission (accounting for 19.5% of the total), which was found to be important in East China where

27 marine vessel shipping activities are intense. Emissions of GEM from natural surfaces were also

28 found to be as important as those from anthropogenic sources for GEM observed at this site.

29 Concurrences of high GOM concentrations with elevated O₃ and temperature, along with the lagged

30　variations of GEM and GOM during daytime demonstrated that the very high GOM concentrations

31　were partially ascribed to intense in situ oxidation of GEM. Strong gas-particle partitioning was also

32　identified when $PM_{2.5}$ was above a threshold value, in which case GOM decreased with increasing

33　$PM_{2.5}$.

34

35　**1. Introduction**

36　　　Mercury (Hg) is a global pollutant of great concerns for environment and human health (Wright

37　et al., 2018). Atmospheric mercury is operationally divided into three forms, i.e. gaseous elemental

38　mercury (GEM), particulate-bound mercury (PBM), and gaseous oxidized mercury (GOM). GEM

39　is the predominant form in the atmosphere (>90%), while GOM and PBM generally have similar

40　concentrations (Xu et al., 2017;Mao et al., 2016). GEM in the atmosphere is relatively stable, having

41　a long lifetime of 0.5-2 year, and can thus transport globally before being oxidized and/or removed

42　from the atmosphere via wet and dry depositions (Schroeder and Munthe, 1998). In contrast, GOM

43　and PBM can be rapidly wiped out from the atmosphere due to their high reactivity and solubility.

44　　　Both natural processes and anthropogenic activities release mercury into the atmosphere

45　(Zhang et al., 2017;Pirrone et al., 2010). Natural sources of mercury include the ocean volatilization,

46　volcanic eruption, evasion from soils and vegetation, geothermal activities, and weathering minerals.

47　Re-emissions of mercury that previously deposited onto the environmental surfaces are also

48　considered as natural sources. As for the anthropogenic emission sources of mercury, coal

49　combustion, non-ferrous smelters, cement production, waste incineration, and mining are

50　considered to be the main sources. After being emitted into the atmosphere, mercury undergoes

51　speciation which plays an important role in its biogeochemical cycle. Previous studies suggest that

52　the oxidation of GEM in the terrestrial environments was generally initiated by O_3 and OH radicals

53　(Mao et al., 2016). Atomic bromine (Br) and bromine monoxide (BrO) are two additional oxidation

54　agents in the marine atmosphere (Tang et al., 2018). Observational studies of GOM in the polar

55　regions (Wang et al., 2009;Ye et al., 2016) and in the subtropical marine boundary layer (Kim et al.,

56　2009) as well as atmospheric modeling studies about mercury cycling (Wang et al., 2016;Zhang et

57　al., 2015) have considered Br to be an important oxidant of GEM. (Wang et al., 2014) even reported

58　that Br is the primary oxidant of GEM in tropical marine boundary layer (MBL). However, it still

59　remains unknown and controversial about the speciation and quantification of the GEM+O_3

products, and the reaction of GEM+OH is still under huge debate between theoretical and experimental studies due to the lacking of mechanisms consistent with thermochemistry (Zhu et al., 2015). The levels of GEM in the atmosphere are mainly controlled by various emission sources, redox reactions, and foliar uptake (Streets et al., 2005;Wright et al., 2016;Zhu et al., 2016). A portion of GOM in air will be adsorbed onto particulate matter due to its high water solubility and relatively strong surface adhesion properties (Liu et al., 2010). The levels of GOM and PBM in the atmosphere, especially in areas far away from anthropogenic mercury sources, are mainly controlled by GEM oxidation processes and atmospheric particulate matter levels, with the former factors affecting the production of GOM and the latter affecting the gas-particle partitioning (Zhang et al., 2013).

Anthropogenic mercury emissions in Asia accounted for more than 50% of the global total mercury emissions (Pacyna et al., 2016), among these approximately 27% were from mainland China (Hui et al., 2017). The Yangtze River Delta (YRD) is one of the most industrialized and urbanized regions in China. Early field measurements in urban Shanghai suggested that TGM was most likely derived from coal fired power plants, smelters and industrial activities (Friedli et al., 2011). Field measurements in urban Nanjing indicated that natural sources were important while most sharp peaks of TGM were caused by anthropogenic sources (Zhu et al., 2012). Modeling studies of atmospheric mercury in eastern China showed that natural emissions, accounting for 36.6% of the total emissions, were the most important source for GEM in eastern China (Zhu et al., 2015). Measurements made at Chongming (an island belonging to Shanghai) observed a downward trend of GEM concentrations from 2014 to 2016, likely caused by the reduction of domestic emissions (Tang et al., 2018). Source apportionment studies for atmospheric mercury are very limited in this region (Zhu et al., 2015), although some studies were made in the other regions of China (Wan et al., 2009;Fu et al., 2019)

In this study, one-year continuous measurements of GEM, GOM, and PBM were conducted at Dianshan Lake Station (DSL), a suburban site in Shanghai. DSL is located in the junction area of Shanghai, Zhejiang, and Jiangsu provinces and is close to the East China Sea (ECS). There are few local mercury sources in this area, making it a unique station for studying the main pollution sources and transport pathways of Hg. The mercury data were analyzed for (1) investigating the impact of meteorology on mercury distribution, (2) exploring the GEM oxidation process, (3) revealing the GOM adsorption process to ambient particles, and (4) identifying potential mercury sources.

90   Knowledge gained from this study provides scientific basis for establishing future mercury emission

91   control policies in this region.

92

93   **2. Materials and methods**

94   **2.1. Site description**

95   Field sampling was conducted on the top of a four-story building (~ 14 m above ground) at a

96   super site (DSL) located in the west area of Shanghai, and nearby the Dianshan Lake in Qingpu

97   district, noting that the lake is the largest freshwater body in Shanghai with a total area of 62 square

98   kilometers (Fig. 1). This supersite is carefully maintained by Shanghai Environmental Monitoring

99   Center (SEMC) and the building is purely used for atmospheric monitoring. There are no large point

100   sources within ~20 kilometers of the site, with the total GEM emissions within a 20 km of the site

101   being estimated as ~100kg/yr. The distance between the sampling site and the coastal lines is ~50

102   km so the site is capable of capturing land-sea circulation. Its special geographical location, i.e. at

103   the junction of Shanghai, Zhejiang and Jiangsu provinces, makes it possible to receive the air masses

104   from all the populous regions. In addition, the site is located at the typical outflow path from East

105   China to the Pacific Ocean. The red dots in Fig. 1 represent the amount of atmospheric Hg emitted

106   by anthropogenic activities in each provinces in 2014 (Wu et al., 2016). The emission intensities of

107   anthropogenic Hg in China were higher in the north and lower in the south. The atmospheric Hg

108   emissions by province in 2014 are listed in Table S1.

109

110   **2.2 Measurements of atmospheric mercury**

111   GEM, GOM, and PBM were measured from June 2015 to May 2016 using the Tekran

112   2537B/1130/1135 system (Tekran Inc., Canada), an instrument that has been widely used worldwide

113   (Landis and Keeler, 2002). In general, GEM, GOM, and PBM in the atmosphere were collected by

114   dual gold cartridges, KCl-coated annular denuder, and regenerable quartz fiber filter, respectively.

115   In this study, GEM was collected at an interval of 5 minutes with a flow rate of 1 L/min, while GOM

116   and PBM were collected at an interval of 2 hours with a flow rate of 10L/min. After the collection,

117   all mercury species were thermally decomposed to Hg^0 immediately and measured by cold vapor

118   atmospheric fluorescence spectroscopy (CVAFS). GEM concentrations were expressed in ng/m^3, while

119   GOM and PBM were in pg/m^3 at standard temperature of 273.14K and pressure of 1013 hPa.

Quality control procedures are strictly followed. The KCl-coated denuder, Teflon coated glass inlet, and impactor plate were replaced weekly and quartz filters were replaced monthly. Before sampling, denuders and quartz filters were prepared and cleaned according to the methods in Tekran technical notes. The Tekran 2537B analyzer was routinely calibrated using its internal permeation source every 47 hours, and was also cross-calibrated every 3 months against an external temperature controlled Hg vapor standard. Two-point calibrations (including zero calibration and span calibration) were performed separately for each pure gold cartridge. Manual injections were performed to evaluate these automated calibrations using the standard saturated mercury vapor. Extremely high concentrations (especially for GOM and PBM) were occasionally observed. If the values were several times higher than the previous hour, those data were regarded as outliers and were excluded in the data analysis.

2.3 Measurements of other air pollutants and meteorological parameters

Water-soluble inorganic anions (SO_4^{2-}, NO_3^-, Cl^-) and cations (K^+, Mg^{2+}, Ca^{2+}, NH_4^+) in $PM_{2.5}$ were simultaneously monitored by the Monitor for Aerosols and Gases in ambient Air (MARGA) at the resolution of one hour. Ambient air was drawn into a sampling box at a flow rate of 16.7L/min. After removing the water-soluble gases by an absorbing liquid, a supersaturation of water vapor induced the particles in the airflow to grow into droplets, and then the droplets were collected and transported into the analytical box which contains two ion chromatograph systems for the determination of the water-soluble ions in $PM_{2.5}$.

Heavy metals (Pb, Fe, K, Ba, Cr, Se, Cd, Ag, Ca, Mn, Cu, As, Hg, Ni, Zn, V) in $PM_{2.5}$ were measured hourly using the Xact-625 Ambient Metals Monitor (Cooper Environmental services, Beaverton, OR, USA), which is a sampling and analyzing X-ray fluorescence spectrometer designed for online measurements of particulate elements. In this study, ambient air was sampled at a flow rate of 16.7L/min and the particles were collected onto a Teflon filter tape. Then the filter tape was moved into the spectrometer, where it was illuminated with an X-ray tube under three excitation conditions and the excited X-ray fluorescence was measured by a silicon drift detector. Daily advanced quality assurance checks were performed during 30 minutes after midnight to monitor shifts in the calibration.

The hourly meteorological data including air temperature, relative humidity (RH), wind speed,

150 and wind direction were simultaneously monitored at the observation site by the automatic weather

151 station (AWS). The data of planetary boundary layer (PBL) height were retrieved from the U.S.

152 National Oceanic and Atmospheric Administration (https://ready.arl.noaa.gov/READYamet.php).

153 Atmospheric ozone (O_3) concentration was continuously measured using Thermo Fisher 49i, which

154 operates on the principle that ozone molecules absorb UV light at a wavelength of 254 nm. The

155 ambient carbon monoxide (CO) and $PM_{2.5}$ concentrations were measured by Thermo Fisher 48Itle

156 and Thermo Fisher 1405F, respectively. All the data were averaged into hour values.

157

158 **2.4 Potential source contribution function (PSCF)**

159 PSCF is a useful tool to diagnose the possible source areas with regard to the levels of air

160 pollutants when setting a contamination concentration threshold at the receptor site. Back trajectory

161 models are used to simulate the airflows. The principle of PSCF is to calculate the ratio of the total

162 number of back trajectory segment endpoints in a grid cell (i, j) exceeding the threshold

163 concentration (m_{ij}) to the total number of back trajectory segment endpoints in this grid cell (i, j)

164 during the whole sampling period (n_{ij}) (Equation (1)) (Schroeder and Munthe, 1998;Cheng et al.,

165 2015):

166 $$\text{PSCF}_{ij} = \frac{m_{ij}}{n_{ij}} \qquad\qquad （1）$$

167 When a particular cell is associated with a small number of endpoint, weighting function (w_{ij})

168 is applied to reduce this uncertainty and the value of w_{ij} is shown in Equation (2) (Fu et al., 2011),

169 in which N_{avg} is the mean n_{ij} of all grid cells with n_{ij} greater than zero. PSCF_{ij} is multiplied by w_{ij} to

170 derive the weighted PSCF values.

171

172 $$w_{ij} = \begin{cases} 1.0, & N_{ij} > 3N_{ave} \\ 0.7, & 3N_{ave} > N_{ij} > 1.5N_{ave} \\ 0.4, & 1.5N_{ave} > N_{ij} > N_{ave} \\ 0.2, & N_{ave} > N_{ij} \end{cases} \qquad （2）$$

173 In this study, we set the threshold concentration as the mean value of the whole sampling period.

174 The mean GEM, PBM, and GOM concentrations were 2.77 ng/m^3, 60.8 pg/m^3, and 82.1 pg/m^3,

175 respectively. The HYSPLIT (HYbrid Single-Particle Lagrangian Integrated Trajectory) model is

176 applied for calculating air mass backward trajectories (Draxler and Rolph, 2012). The model was

177 run online at the NOAA ARL READY Website using the meteorological data archives of Air

178   Resource Laboratory (ARL). The meteorological input data used in the model was obtained from

179   NCEP (National Centers for Environmental Prediction)'s global data assimilation system (GDAS)

180   with a horizontal resolution of $0.5° \times 0.5°$. In this study, 72-hours back trajectories were calculated

181   at 500m AGL (above ground level) and the cell size was set as $0.5° \times 0.5°$.

182

2.5 Positive matrix factorization (PMF)

184   The PMF model is widely used to quantitatively determine the source contributions of specific

185   air pollutants (Gibson et al., 2015). The essential principle of PMF is that the concentration of each

186   sample is determined by source profiles and different contributions. The equation of the PMF model

187   is shown as Equation (3):

188
$$X_{ij} = \sum_{k=1}^{P} g_{ik} f_{kj} + e_{ij} \qquad\qquad (3)$$

189   Where X_{ij} is the concentration of the jth contamination at the receptor site in the ith sample. g_{ik}

190   represent the contribution of the kth factor on the ith sample, f_{kj} is used to express the mass fraction

191   of the jth contamination in the kth factor, P is the number of factors, which represent pollution

192   sources, and e_{ij} is the residual for each measurement or model error.

193   Before the model determines the optimal non-negative factor contributions and factor profiles,

194   an objective function, which is the sum of the square difference between the measured and modeled

195   concentrations weighted by the concentration uncertainties, has to be minimized (Cheng et al., 2015).

196   The equation that determines the objective function is given by Equation (4):

197
$$Q = \sum_{i=1}^{n} \sum_{j=1}^{m} \left(\frac{X_{ij} - \sum_{k=1}^{p} A_{ik} F_{kj}}{S_{ij}} \right)^2 \qquad\qquad (4)$$

198   where X_{ij} is the ambient concentration of the jth pollutant in the ith sample (m and n represent the

199   total number pollutants and samples, respectively). A_{ik} is the contribution of the kth factor on the ith

200   sample and F_{kj} is the mass fraction of the jth pollutant in the kth factor. S_{ij} is the uncertainty of the

201   jth pollutant on the ith measurement, and P is the number of factors, which imply the pollutant

202   sources. In this study, the number of factors from 3 to 8 was examined with the optimal solutions

203   determined by the slope of the Q value versus the number of factors. For each run, the stability and

204   reliability of the outputs were assessed by referring to the Q value, residual analysis, and correlation

205   coefficients between observed and predicted concentrations. Finally, a 6-factor solution, which

206   showed the most stable results and gave the most reasonable interpretation, was chosen. Before

207   running the model, a dataset including unique uncertainty values of each data point was created and

208   digested into the model. The error fraction was assumed to be 15% of concentrations for GEM and

209   10% of concentrations for the other compounds (Xu et al., 2017), the missing data were excluded

210   and the total number of samples was 3526.

211

212   **3. Results and discussion**

213   **3.1. Characteristics of atmospheric mercury species**

214   Fig. 2 displays the time series of atmospheric GEM, PBM, and GOM concentrations during 1

215   June, 2015 to 31 May, 2016 at DSL. The annual average concentrations of GEM, PBM, and GOM

216   at DSL were 2.77 ± 1.36 ng/m^3, 60.8 ± 67.4 pg/m^3, and 82.1 ± 115.4 pg/m^3, respectively. As shown in

217   Table 1, the levels of GEM and PBM in this study were lower than at some sites in China by a factor

218   of 2-7, such as rural Miyun, suburban Xiamen, and urban Guiyang (Xu et al., 2015;Fu et al., 2011).

219   However, compared to the studies conducted in urban and rural areas abroad such as New York

220   (Wang et al., 2009), Chicago (Gratz et al., 2013), and Nova Scotia (Cheng et al., 2014b), the

221   concentrations of GEM and PBM in the suburbs of Shanghai were much higher by a factor of 1-3

222   and 3-8, respectively. Different from GEM and PBM, the GOM concentrations at DSL were higher

223   than at all the other Chinese sites and sites around the world listed in Table 1. The mean GOM

224   concentration in this study (82.1 pg/m^3) was even higher than that in Guiyang (35.7 pg/m^3), where

225   the emissions of GEM and GOM were quite intense due to the massive primary emission sources

226   such as coal-fired power plants and cement plants (Fu et al., 2011). The abnormally high GOM

227   concentrations observed in this study were likely dominated by strong primary emissions.

228   The monthly patterns of GEM, PBM, and GOM during the whole sampling period are shown

229   in Fig. 3. The seasonal mean GEM concentrations were slightly higher in winter (2.88 ng/m^3) and

230   summer (2.87 ng/m^3) than in spring (2.73 ng/m^3) and autumn (2.63 ng/m^3), with the highest monthly

231   mean value of 3.19 ng/m^3 in June and the lowest of 2.39 ng/m^3 in March. Statistical test showed that

232   no significant differences of the seasonal variations of GEM concentrations among spring, summer,

233   and winter were observed (Table S2). This was different from many urban and remote sites in China,

234   such as Guiyang, Xiamen, and Mt. Changbai, where GEM showed significantly high concentrations

235   in cold than warm seasons (Wang et al., 2016;Xu et al., 2015;Fu et al., 2012). The relatively high

236   GEM concentrations during the cold season in China should be attributed to the increases of energy

237   consumption (Fu et al., 2015). In this study, GEM concentration in summer was comparable to that

238 in winter, which was likely attributed to the strong natural mercury emissions (e.g. soils, vegetations,

239 and water) due to the elevated temperature in summer (Liu et al., 2016). The seasonal mean PBM

240 concentrations were the highest in winter (93.5 pg/m^3) while the lowest in summer (35.7 pg/m^3),

241 and moderate in autumn (56.8 pg/m^3) and spring (51.6 pg/m^3), with the highest monthly mean value

242 of 109.4 pg/m^3 in January and the lowest of 28.9 pg/m^3 in September. This seasonal pattern was

243 consistent with those at the other sites in China such as Beijing and Nanjing (Kim et al., 2009;Lynam

244 and Keeler, 2005). PBM concentrations at low altitude sites in the Northern Hemisphere were

245 commonly enhanced in winter, which was ascribed to intense emissions from residential heating,

246 the reduction of wet scavenging processes, enhanced gas-particle partitioning of atmospheric

247 mercury under low temperature, etc. (Rutter and Schauer, 2007). As for GOM, its seasonal mean

248 concentrations were the highest in winter (124.0 pg/m^3), followed by summer (77.3 pg/m^3), spring

249 (68.1 pg/m^3), and autumn (61.0 pg/m^3). GOM concentrations in summer were much lower than that

250 in winter, but were higher than in spring and autumn. Secondary transformation from GEM in

251 warm/hot seasons and slow dispersion in winter can explain such season variations, as further

252 discussed below.

253   Fig. 4 shows the diurnal variations of GEM, PBM, and GOM during the whole sampling period.

254 To ensure the time resolutions were consistent among all the three mercury species, the temporal

255 resolution of measured GEM was converted from 5 minutes to the two-hour average. As shown in

256 Fig. 4, GEM concentrations were higher during daytime with the maximum in the morning at around

257 10:00 and minimum in the midnight at around 02:00. The diurnal trends of GOM were similar to

258 that of GEM, except that the minimum GOM occurred at around 20:00 in the evening. The diurnal

259 trends of PBM were different from those of GEM and GOM, exhibiting relatively higher

260 concentrations during nighttime. The PBM maximum occurred in the early morning at around 6:00

261 and the minimum in the afternoon at 18:00. The diurnal trends of GEM, PBM, and GOM were

262 similar to those observed in Nanjing (Zhu et al, 2012), but different from those in Guiyang, Xiamen,

263 and Guangzhou (Wang et al., 2016;Chen et al., 2013). Since DSL and Nanjing both belong to the

264 Yangtze River Delta region, the similar meteorology and emission characteristics within the Yangtze

265 River Delta region may explain the similar diurnal patterns of Hg species between these two sites.

266 The elevated GEM concentrations at DSL during daytime were likely related to the stronger

267 emissions from both human activities and natural releases. GOM and GEM showed similar diurnal

268 variations and both peaked at 10:00, probably suggesting that GOM and GEM were affected by

269 common sources (e.g. coal-fired power plants and industrial boilers). The high PBM concentrations

270 at night were likely derived from the adsorption of Hg species onto the preexisting particles and the

271 subsequent accumulation in the shallow nocturnal boundary layer. Wind speed was relatively low

272 while relative humidity was high at night, which were conducive to the adsorption of GOM onto

273 the particles (Fig. 4).

274

275 **3.2. Relationship between Hg species and meteorological factors**

276 Fig. 5 shows the relationship between wind direction/speed and atmospheric mercury species.

277 One-third of the prevailing winds came from the east and 16% from the north at DSL during the

278 study period (Fig. 5a). Wind speed from all directions during the study period was mainly in the

279 range of 0-6 m/s, of which wind speed higher than 4 m/s mainly derived from the east. The highest

280 GEM concentrations, averaged at 3.92 ng/m^3, were linked to the winds from the south and southwest,

281 in comparison of the average concentration of 2.71 ng/m^3 from the other wind sectors (Fig. 5b). A

282 similar wind-concentration pattern was also seen for GOM, but not for PBM for which high

283 concentrations were from the north/northwest and south/southwest (Fig. 5c &5d). Anthropogenic

284 emissions were generally higher in northern than southern China (Fig 1), which explained largely

285 the observed high concentrations from the north wind sector. However, even higher atmospheric Hg

286 concentrations were observed from the south and southeast wind sector, implying other factors

287 dominated the Hg concentrations in these wind sectors. (Wang et al., 2016) reported that Hg

288 concentrations in the surface soils were generally higher in southern than northern China. A

289 modeling study estimated that the mean annual Hg air-soil flux in the southwest region of our

290 sampling site (e.g. Zhejiang province) ranged from 8.75 to 15 ng m^{-2} h^{-1}, while that in the

291 north/northwest region (e.g. Jiangsu province) ranged from 2.5 to 8.75 ng m^{-2} h^{-1} (Wang et al., 2016).

292 Hence, emissions from natural sources, such as soils, vegetations and water, should play important

293 roles in the observed high atmospheric Hg concentrations from the south to southeast wind sectors.

294 In order to confirm this hypothesis, the relationship between temperature and Hg

295 concentrations at DSL was investigated. Seasonal temperature in ascending order was divided into

296 different groups and the corresponding mean Hg concentrations are plotted in Fig. 6. In spring,

297 GEM concentration increased with increasing temperature. In the other seasons, similar trends were

observed when temperature increased to a certain value. Such a phenomenon was likely caused by temperature-dependent surface emissions, noting that the increasing PBL height with increasing temperature should have offset some of the increased mercury concentration. GOM concentration showed a clearly positive correlation with temperature in summer, largely due to the in situ oxidation of GEM under high temperature heavy ozone pollution (Qin et al., 2018). Such a good correlation did not exist in the other seasons. As for PBM, it appeared to have weakly negative correlation with PBL height, suggesting the atmospheric diffusion conditions were influential on the concentrations of PBM.

3.3. Source-apportionment analyses

3.3.1. Potential source regions for mercury

PSCF analysis results suggested that the potential sources for GEM were mainly located in Anhui, Jiangxi, and Zhejiang provinces, and also possibly in Shandong province (Fig. 7a). Seasonal dominant sources affecting GEM at DSL site were those in Jiangsu and Zhejiang provinces in spring, in Anhui and Jiangxi provinces in summer, In Jiangsu province in autumn, and in Anhui and Zhejiang provinces in winter (Fig. S1). In addition, sources in Henan and Shandong provinces seemed to also play a role on GEM in winter, suggesting the importance of long-range transport in this season. There existed substantial high PSCF signals in the southern areas, stronger than those in the northern areas, despite lower anthropogenic emissions in the south. For example, southern provinces such as Zhejiang and Jiangxi were estimated to release 25 tons/yr atmospheric Hg from anthropogenic activities (Fig. 1), far less than those from the northern provinces such as Jiangsu and Shandong (77 tons/yr) (Wu et al., 2016). Based on the mean annual Hg air-soil flux of 8.75 to 15 ng m^{-2} h^{-1} in the southwest region of our sampling site (Wang et al., 2016), it was estimated that the total Hg emissions from soils were in the range of 6.9 - 13.9 tons/yr from Zhejiang province, which was comparable to the anthropogenic Hg emission of approximately 15tons/yr in 2014 in this province (Wu et al., 2016). Thus, the soil emission of GEM from natural surfaces was an importance source in southern areas, corroborating the discussion in Section 3.2. In addition, the East China Sea (including the offshore areas and open ocean) showed sporadic high PSCF signals of GEM in all the four seasons (Fig. S1), indicating possible influences from shipping activities (more discussion below).

328   The PSCF pattern of PBM was quite different from that of GEM (Fig. 7b). The annual potential

329   source regions for PBM were mainly from the northern areas of Jiangsu and Anhui provinces, and

330   from the northeastern China including Shandong and Hebei provinces. These provinces were

331   regarded as the main Hg sources areas in China and accounted for approximately 25.2% of the

332   Chinese anthropogenic atmospheric Hg emissions (Wu et al., 2016). Seasonal sources for PBM were

333   similar in spring, autumn, and winter, but not in summer for which high PSCF values were mainly

334   located in the southern areas of Shanghai, likely due to the prevailing winds in summer from the

335   south, southeast, and southwest where Zhejiang and Jiangxi provinces were important mercury

336   source regions.

337   The annual potential sources for GOM were mainly located in Anhui and Zhejiang provinces

338   and the coastal areas along Jiangsu province (Fig. 7c). The PSCF pattern of GOM was similar to

339   that of GEM but not PBM. The potential source regions of GOM were more from southern than

340   northern China, likely due to the higher atmospheric oxidant levels in the southern regions. Seasonal

341   PSCF patters for GOM showed dominant sources in Zhejiang and Jiangxi provinces in summer,

342   major sources in inland areas and moderate sources over the East China Sea and Yellow Sea in

343   spring, major sources in Zhejiang province and moderate sources over the Yellow Sea in autumn,

344   and major sources from the coastal areas of Jiangsu to a vast ocean of the Yellow Sea in winter. One

345   previous study suggested that the marine boundary layer could provide considerable amounts of

346   oxidants such as chlorine and bromine, which were beneficial for the production of GOM by

347   oxidizing GEM (van Donkelaar et al., 2010) and this mechanism may explain the substantial PSCF

348   signals over the ocean.

349   The PSCF analysis results discussed above demonstrated the relative contributions from the

350   short-range transport from the adjacent areas of Shanghai, and regional and long-range transport

351   from northern and southern China as well as from the ocean on contributing to speciated

352   atmospheric mercury at DSL (more discussion below).

353

354   **3.3.2. Quasi-local sources versus regional/long-range transport on atmospheric mercury**

355   According to the relationships between wind direction and Hg concentration as well as the

356   PSCF analysis results discussed above, the elevated GEM, GOM, and PBM concentrations at DSL

357   were generally associated with the wind sectors from the southwest and north directions. To reveal

the relative importance of local sources and regional transport, the ratio of GOM/PBM was applied

as an indicator based on the fact that the residence time of GOM is generally considered to be shorter

than that of PBM (Lee et al., 2016). Lower ratios of GOM/PBM indicate the dominance of

regional/long-range transport over local sources, and vice versa. In the following discussion, the

ratios of GOM/PBM during the whole study period were grouped into four categories, i.e. 0-1, 1-2,

2-3, and higher than 3 with their corresponding wind sector distribution shown in Fig. 8. Higher

GOM/PBM ratios were mostly associated with winds from the east and southeast, e.g., with the

frequency of these two wind sectors increased from 27% for the GOM/PBM ratios of less than 1 to

52% for the ratios higher than 3. Winds from these wind sectors were typically characterized of

relatively clean air masses, suggesting the dominance of local sources over the regional transport at

the observational site. In contrast, lower GOM/PBM ratios were mostly associated with winds

clockwise from the west to the north, with the frequency of these wind sectors decreased

significantly from 44% for the GOM/PBM ratios less than 1 to 21% for the ratios higher than 3,

indicating the importance of the long-range/regional transport from northern China associated with

the relatively low GOM/PBM ratios. According to the PSCF results above, the potential source areas

of Hg species (GEM, GOM and PBM) derived mostly from the south and southwest of the sampling

site. As shown in Fig. 8, the frequency of south, southwest, west, and northeast winds showed no

clear trend as the GOM/PBM ratios increased, suggesting complicated interactions that cannot be

explained solely by the local sources or regional transport. In general, the GOM/PBM ratio can be

used as a qualitative tracer for identifying the relative importance of long-range transport vs. local

sources if one factor dominates over the other.

The relationships among GEM, CO, secondary inorganic aerosols (SNA) and GOM/PBM ratio

were further investigated. Fig. 9 displays the concentrations of GEM as a function of GOM/PBM

ratio colored by CO. The size of the circles represents the corresponding concentration of SNA in

$PM_{2.5}$. CO has been commonly used as a tracer of fuel combustion, and SNA were derived from

secondary particle formation via the gas-to-particle conversion. CO and SNA were collectively used

as proxies of the extent of regional/long-range transport of anthropogenic air pollutants. As shown

in Fig. 9, GEM generally increased with increasing GOM/PBM ratio. In addition, lower GOM/PBM

ratios were associated with higher CO and SNA concentrations and vice versa. This corroborated

the discussion above that the GOM/PBM ratio was a reliable tracer for assessing the relative

388   importance of regional/long-range transport vs. local atmospheric processing.

389   GEM concentration fluctuated with a mean value of less than 2.6 ng/m^3 when the GOM/PBM

390   ratio is less than 2.5, increased from 2.61 ng/m^3 in the GOM/PBM ratio bin of 2.5-3.0 to 2.8 ng/m^3

391   in the bin of 3.0-3.5, and then remained relatively stable when the GOM/PBM ratio is higher than

392   3.0. Generally, GEM showed an increasing trend as the GOM/PBM ratio increased while both SNA

393   and CO decreased. The elevated GEM concentrations tended to be associated with quasi-local

394   sources. In contrast, under the high SNA and CO conditions and when GOM/PBM ratios were lower,

395   GEM showed relatively low concentrations, suggesting that regional/long-range transport didn't

396   favor the elevation of GEM concentration. It has been recognized that the common regional/long-

397   range transport pathways contributing to the particulate pollution events in Shanghai were from the

398   north and northwest, which were originating mostly from the North China Plain. The relatively

399   lower GEM concentrations under the regional/long-range transport conditions corroborated the

400   PSCF analysis that only moderate probabilities of GEM source regions were from northern China

401   (Fig. 7a).

402

3.3.3. Source apportionment by the combined PMF and PCA analyses

404   PMF modeling has been widely used to apportion the sources of atmospheric pollutants. In this

405   study, GEM together with heavy metals and soluble ions, measured online synchronously, were

406   introduced into the EPA PMF5.0 model to apportion the major anthropogenic sources of GEM. A

407   six-factor solution was selected based on the results of multiple model runs, which can well explain

408   the measured concentrations of the introduced species. The profiles of the six identified PMF factors

409   and contributions of major anthropogenic sources to GEM are shown in Fig. 10. It has to be noted

410   that since no tracers for the natural emissions (e.g. soil, vegetation, and ocean) were available in this

411   study, the identification of natural mercury sources was not possible based on the PMF modeling.

412   Factor 1 had high loadings of Se, As, Pb, NO$_3^-$, SO$_4^{2-}$, and NH$_4^+$. Se, As, and Pb were typical

413   tracers of coal combustion. SO$_4^{2-}$ and NO$_3^-$ were also formed from the gaseous pollutants emitted

414   from coal burning. Hence, this factor was defined as coal combustion sources and accounted for

415   12.3% of the anthropogenic GEM. Fig. S4 plotted wind roses of specific aerosol species. SO$_4^{2-}$ and

416   As shared similar patterns with high concentrations mainly from the southwest. Since combustion

417   was an important source of GEM, this confirmed that the major sources of GEM were located in the

418   southwest region.

419   Factor 2 displayed particularly high loadings of Ni and V. The major sources of Ni in the

420   atmosphere can be derived from coal and oil combustions (Tian et al., 2012), and oil combustion

421   accounted for 85% of anthropogenic V emissions in the atmosphere (Duan and Tan, 2013). In

422   general, Ni and V have been considered as good tracers of heavy oil combustion, which has been

423   commonly used in marine vessels (Viana et al., 2009). Thus, this factor was identified as shipping

424   emissions. The sampling site is adjacent to the East China Sea and is located in Shanghai which has

425   the largest port in the world. Fig. S4 showed similar patterns of Ni and V with high concentrations

426   mainly from the northeast, east, and southeast. To further validate this factor, the time-series of GEM

427   concentrations from the shipping factor based on the PMF modeling were extracted and digested

428   into the PSCF modeling (Fig. S5), which showed that the potential sources regions were mainly

429   located over the East China Sea and coastal regions. This indicated factor 2 from PMF should be

430   representative of the shipping sector as well as oil combustion in motor vehicles and inland shipping

431   activities. Overall, this factor accounted for 19.6% of anthropogenic GEM and ranked as the second

432   largest emission sector, highlighting the urgent need of controlling the marine vessel emissions.

433   Factor 3 showed high loadings of Ca and moderate loadings of Ba and Fe. Ca and Fe are rich

434   elements in crust that can be used for cement production. As mercury could be released during

435   industrial processes of cement production, Factor 3 was assigned as cement production and

436   accounted for a minor fraction of 6.3 % of the anthropogenic GEM.

437   Factor 4 was characterized by high loadings of Cr and moderate loadings of Mn, Fe, Ni, and

438   Cu. These species together served as markers of metals smelting. Metals smelting were known to

439   be large sources of Hg emitted to the atmosphere (Pirrone et al., 2010), especially in the YRD, one

440   of the most developed and industrialized areas in China. This factor accounted for 7.6% of the

441   anthropogenic GEM.

442   Factor 5 had high loadings of Cl$^-$. Waste incineration is an important source of enriched

443   chloride over land. Factor 5 was identified to be waste incineration, which contributed 6.4% of the

444   anthropogenic GEM.

445   Factor 6 was characterized by high loadings of Cd, Ag, K$^+$, and Na$^+$. The major sources of Cd

446   in China were iron and steel smelting industries (Duan and Tan, 2013). Ag was mainly used in

447   industrial applications, including electronic appliances and photographic materials. K$^+$ was a typical

tracer of biomass burning, which often stemmed from agriculture waste burning over the Yangtze River Delta and the North China Plain. Factor 6 was considered as a combined source of the industrial and biomass burning emission sectors. It was estimated to contribute 47.8% of the anthropogenic GEM.

As discussed above, surface emissions were likely to be important sources of the observed atmospheric mercury. As PMF modeling didn't resolve the natural sources of mercury, the PCA (Principal Component Analysis) was applied for further source apportionment by introducing the temperature parameter. Four factors are resolved, which totally explained 75.32% of the variance as shown in Table 2. Factor 1 accounted for 34.15% of the total variance with high loadings for SO_2, SO_4^{2-}, NH_4^+, K^+, Pb, Se, and As, which was explained as coal combustion mixed with biomass burning. Factor 2 accounted for 14.85% of the total variance with high loadings for temperature, O_3, and NH_3, which was explained as surface emissions. Factor 3 accounted for 13.43% of the total variance and showed high loadings for Ni and V, which indicated the contribution of ship emissions. Factor 4 accounted for 12.89% of the total variance and showed high loading for Fe and Ca, indicating the contribution of cement production.

3.4. Factors affecting the formation and transformation of mercury species

3.4.1. Factors affecting the formation of GOM

A typical case from July 24 to July 27, 2015 was chosen to investigate the possible formation process of GOM. As shown in Fig. 11, the shaded episodes represented nighttime from 18:00 to 6:00 the next day. Both GEM and GOM exhibited rising trends during nighttime (Fig. 11a), which was ascribed to nighttime accumulation effect due to the very shallow boundary layer (Fig. 11c). Starting from 6:00 in the morning, GEM concentration began to gradually decline as the boundary layer developed. In contrast, the concentration of GOM continued to rise from 6:00 until it reached the peak value at around 10:00. During this period, ozone and temperature also kept rising until surpassed 200 μg/m^3 and 34°C, respectively. Accordingly, as an anthropogenic emitting tracer, the concentration of carbon monoxide was basically stable and even showing a downward trend, which suggested that some other factors caused the increase of GOM in addition to the anthropogenic emissions. This phenomenon clearly revealed the acceleration of the conversion process of GEM to

478   GOM under favorable atmospheric conditions of higher O_3 concentration and ambient temperature.

479   In the case of atmosphere dilution by the rise of PBL, the fact that GOM was not falling but rising

480   suggested the great influence of this process on ambient GOM concentration. Similar observation

481   has been found at the high-altitude Pic du Midi observatory in southern France (Fu et al., 2016),

482   which was almost impervious to anthropogenic emission sources. The important role of GEM

483   oxidation in our sampling site, which is located in one of the most developed industrial areas in

484   China, was most likely due to the presence of sufficient oxidants in this area. Severe ozone pollution

485   frequently occurred in the YRD due to strong anthropogenic emission intensities (Duan et al., 2017).

486   Previous studies suggested that the primary oxidants in the terrestrial environment were O_3 and OH

487   radicals (Zhang et al., 2015), while Br was an important oxidant in the subtropical marine boundary

488   layer (Obrist et al., 2011). It was possible that, in addition to O_3 and OH radicals, Br might also be

489   an important species to oxidize GEM as the DSL site is adjacent to the East China Sea.

490   Statistical relationships among GOM, O_3, and temperature are shown in Fig. 12. Temperature

491   was plotted against a range of GOM/PBM bins colored by O_3 and the size of the circles represents

492   the concentration of GOM. In general, as temperature and O_3 increased, the concentration of GOM

493   was subject to substantial enhancement. For instance, when temperature (O_3) was below 12°C (65.7

494    $\mu g/m^3$), GOM was averaged at 37.8 pg/m^3. While temperature (O_3) increased to above 20°C (91.5

495    $\mu g/m^3$), GOM rose to 168.8 pg/m^3, yielding a factor of 1- 5 increases. This further confirmed the

496   hypothesis from the case study above that the levels of oxidants under favorable environmental

497   conditions were crucial for the formation of GOM. It can also be seen from Fig. 12 that the lower

498   ratios of GOM/PBM were associated with lower temperatures and O_3 concentrations, indicating

499   relatively weak photochemistry during the cold seasons. On the contrary, the higher ratios of

500   GOM/PBM were associated with higher temperature and O_3 concentrations, indicating relatively

501   strong photochemistry during the warm seasons. Thus, the formation of GOM was more favored by

502   local atmospheric processing rather than the transport. This study demonstrated the abnormally high

503   GOM concentrations observed at DSL were largely ascribed to local oxidation reactions. However,

504   the explicit formation mechanism of GOM need to be investigated by measuring more detailed

505   components of GOM and atmospheric oxidants.

506

507   **3.4.2. Factors affecting the transformation of PBM**

508   Previous studies have shown that PBM can be emitted directly from various anthropogenic

509   sources such as coal-fired power plants and industries (Cheng et al., 2014a;Wu et al., 2016).   In

510   addition, gas-particle partitioning was considered to be an important pathway for the formation of

511   PBM (Zhang et al., 2015;Amos et al., 2012). Since most of the areas in the YRD belong to non-

512   attainment areas in regard of particulate pollution and the concentrations of GOM were particularly

513   high at DSL as discussed above, the role of gas-particle partitioning in the formation of PBM should

514   be investigated. Previous studies reported that the concentrations of $PM_{2.5}$ in eastern and northern

515   China are highest in the world (van Donkelaar et al., 2010), for which the elevated atmospheric

516   particulate matter probably facilitates the formation of PBM (Fu et al., 2015). Fig. 13 shows the

517   statistical pattern of the variation of PBM and GOM in the ascending bins of $PM_{2.5}$. The

518   concentration of PBM increased with increasing $PM_{2.5}$, likely due to the gas-particle portioning of

519   oxidized Hg (Amos et al., 2012;Cheng et al., 2014a). The trend of GOM was somehow different

520   from that of PBM. When $PM_{2.5}$ concentrations were at relatively low levels under 75 $\mu g/m^3$, GOM

521   concentrations increased with $PM_{2.5}$. However, when $PM_{2.5}$ concentrations increased to 75-105

522    $\mu g/m^3$, GOM exhibited a clear decreasing trend as $PM_{2.5}$ increased. This suggests that low levels

523    $PM_{2.5}$ may not have an apparent effect on GOM, but higher levels of $PM_{2.5}$ may directly affect GOM

524   through adsorption of GOM onto the particles. When $PM_{2.5}$ concentrations exceeded 105 $\mu g/m^3$,

525   GOM exhibited a slightly increasing trend as $PM_{2.5}$ increased. High $PM_{2.5}$ concentrations in China

526   always related to severe anthropogenic emissions (van Donkelaar et al., 2010), so the moderate

527   increasing trend of GOM in these bins should be attributed to the impact of strong primary emissions.

528   A short episode from December 30, 2015 to January 1, 2016 was chosen to further investigate

529   this phenomenon. As shown in Fig. 14, in Stage 1, the concentrations of $PM_{2.5}$ were below 100

530    $\mu g/m^3$, PBM and GOM shared the similar temporal variation as $PM_{2.5}$. In Stage 2, as $PM_{2.5}$ kept

531   climbing, GOM began to show somewhat negative correlation with $PM_{2.5}$, but not significant. The

532   reason might be that the relatively high temperature and low humidity during this period were not

533   conducive to the transfer of GOM to particle matters. In Stage 3, GOM decreased as $PM_{2.5}$ continued

534   to increase, showing a clear anti-correlation. During this period, PBM showed a consistent trend

535   with $PM_{2.5}$ and CO. Temperature was relatively low but with relatively high humidity. This

536   phenomenon clearly demonstrated the process of gas-particle partitioning of PBM formation. In

537   stage 4, GOM and PBM showed similar decreasing trend with $PM_{2.5}$ and CO. The low GOM

concentrations, low humidity, and high temperature resulted in no significant signs of GOM adsorption to $PM_{2.5}$ in this stage. In general, under high $PM_{2.5}$, GOM concentration and humidity, and low temperature conditions at DSL, clear processes of gas-particle partitioning were observed.

4. Conclusions

In this study, a year-long observation of speciated atmospheric Hg concentrations was conducted at the Dianshan Lake (DSL) Observatory, located on the typical transport routes from mainland China to the East China Sea. Different from many sites in China, GEM at DSL exhibited high concentrations in winter, summer, and spring, which was due to the strong re-emission fluxes from natural surfaces in summer and enhanced coal combustion for residential heating over northern China in winter. The relatively high GOM concentrations in summer indicated that the formation of GOM from GEM oxidation was likely crucial. PBM exhibited high concentrations in winter, indicating the impact of long-range transport. The diurnal patterns of GEM and GOM were similar with relatively high levels during daytime. For GEM, this was likely attributed to both human activities and re-emission from natural surfaces during daytime. For GOM, in addition to direct emissions, high concentrations during daytime were partially ascribed to photochemical oxidation of GEM. The PBM concentrations were higher during nighttime, which was ascribed to the accumulation effect within the shallow nocturnal boundary layer.

The relationship between meteorological factors and atmospheric Hg species showed that the high Hg concentrations were generally related to the winds from the south, southwest, and north and positively correlated with temperature. Both anthropogenic sources and natural sources contributed to the atmospheric mercury pollution at DSL. Higher GOM/PBM ratios corresponded to lower CO and SNA concentrations and vice versa. The ratio of GOM/PBM can be used as a tracer for distinguishing local sources and regional/long-range transport based on the fact that the residence time of GOM was shorter than that of PBM. GEM as a function of the GOM/PBM ratio indicated that when the quasi-local sources dominated, GEM concentrations were relatively higher than those events under the regional/long-range transport conditions. According to the PMF source apportionment results, six sources of anthropogenic GEM and their contributions were identified, i.e. industrial and biomass burning (47.8%), shipping emission (19.6%), coal combustion (12.3%), iron and steel production (7.6%), incineration (6.4%), and cement production (6.3%). The

568 significant contribution of shipping emission suggested that in coastal areas mercury emitted from

569 marine vessels can be significant. In addition, a considerable natural source of GEM was identified

570 by digesting temperature into the principle component analysis.

571   The formation processes of GOM and PBM based on episodic studies were also investigated.

572 The high GOM concentrations were partially attributed to strong local photochemical reactions

573 under the conditions of high O_3 and temperature. Under high $PM_{2.5}$ concentration and humidity and

574 low temperature conditions, the gas-particle partitioning processes were observed.

575

576 **Author contributions.** XQ, KH, and CD conceived the study and wrote the paper. XW, YL, and

577 DW performed the measurements and collected data. All have contributed to the data analysis and

578 review of the manuscript.

579

585

586 **References**

587 Amos, H. M., Jacob, D. J., Holmes, C. D., Fisher, J. A., Wang, Q., Yantosca, R. M., Corbitt, E. S.,

588   Galarneau, E., Rutter, A. P., Gustin, M. S., Steffen, A., Schauer, J. J., Graydon, J. A., Louis, V. L.

589   S., Talbot, R. W., Edgerton, E. S., Zhang, Y., and Sunderland, E. M.: Gas-particle partitioning of

590   atmospheric Hg(II) and its effect on global mercury deposition, Atmos. Chem. Phys., 12, 591-603,

591   10.5194/acp-12-591-2012, 2012.

592 Chen, L. G., Liu, M., Xu, Z. C., Fan, R. F., Tao, J., Chen, D. H., Zhang, D. Q., Xie, D. H., and Sun, J. R.:

593   Variation trends and influencing factors of total gaseous mercury in the Pearl River Delta-A highly

594   industrialised region in South China influenced by seasonal monsoons, Atmospheric Environment,

595   77, 757-766, 10.1016/j.atmosenv.2013.05.053, 2013.

596 Cheng, I., Zhang, L., and Blanchard, P.: Regression modeling of gas-particle partitioning of atmospheric

597   oxidized mercury from temperature data, J. Geophys. Res.-Atmos., 119, 11864-11876,

598   10.1002/2014jd022336, 2014a.

599 Cheng, I., Zhang, L. M., Mao, H. T., Blanchard, P., Tordon, R., and Dalziel, J.: Seasonal and diurnal

600   patterns of speciated atmospheric mercury at a coastal-rural and a coastal-urban site, Atmospheric

601   Environment, 82, 193-205, 10.1016/j.atmosenv.2013.10.016, 2014b.

602 Cheng, I., Xu, X., and Zhang, L.: Overview of receptor-based source apportionment studies for speciated

atmospheric mercury, Atmos. Chem. Phys., 15, 7877-7895, 10.5194/acp-15-7877-2015, 2015.

Draxler, R., and Rolph, G.: HYSPLIT - Hybrid Single Particle Lagrangian Integrated Trajectory Model, 2012.

Duan, J., and Tan, J.: Atmospheric heavy metals and Arsenic in China: Situation, sources and control policies, Atmospheric Environment, 74, 93-101, 10.1016/j.atmosenv.2013.03.031, 2013.

Duan, L., Wang, X. H., Wang, D. F., Duan, Y. S., Cheng, N., and Xiu, G. L.: Atmospheric mercury speciation in Shanghai, China, Sci. Total Environ., 578, 460-468, 10.1016/j.scitotenv.2016.10.209, 2017.

Friedli, H. R., Arellano, A. F., Geng, F., Cai, C., and Pan, L.: Measurements of atmospheric mercury in Shanghai during September 2009, Atmospheric Chemistry and Physics, 11, 3781-3788, 10.5194/acp-11-3781-2011, 2011.

Fu, X., Maruszczak, N., Heimbürger, L.-E., Sauvage, B., Gheusi, F., Prestbo, E. M., and Sonke, J. E.: Atmospheric mercury speciation dynamics at the high-altitude Pic du Midi Observatory, southern France, Atmospheric Chemistry and Physics, 16, 5623-5639, 10.5194/acp-16-5623-2016, 2016.

Fu, X. W., Feng, X. B., Qiu, G. L., Shang, L. H., and Zhang, H.: Speciated atmospheric mercury and its potential source in Guiyang, China, Atmospheric Environment, 45, 4205-4212, 10.1016/j.atmosenv.2011.05.012, 2011.

Fu, X. W., Feng, X., Shang, L. H., Wang, S. F., and Zhang, H.: Two years of measurements of atmospheric total gaseous mercury (TGM) at a remote site in Mt. Changbai area, Northeastern China, Atmospheric Chemistry and Physics, 12, 4215-4226, 10.5194/acp-12-4215-2012, 2012.

Fu, X. W., Zhang, H., Yu, B., Wang, X., Lin, C. J., and Feng, X. B.: Observations of atmospheric mercury in China: a critical review, Atmospheric Chemistry and Physics, 15, 9455-9476, 10.5194/acp-15-9455-2015, 2015.

Fu, X. W., Zhang, H., Feng, X. B., Tan, Q. Y., Ming, L. L., Liu, C., and Zhang, L. M.: Domestic and Transboundary Sources of Atmospheric Particulate Bound Mercury in Remote Areas of China: Evidence from Mercury Isotopes, Environmental science & technology, 53, 1947-1957, 10.1021/acs.est.8b06736, 2019.

Gibson, M. D., Haelssig, J., Pierce, J. R., Parrington, M., Franklin, J. E., Hopper, J. T., Li, Z., and Ward, T. J.: A comparison of four receptor models used to quantify the boreal wildfire smoke contribution to surface PM2.5 in Halifax, Nova Scotia during the BORTAS-B experiment, Atmospheric Chemistry and Physics, 15, 815-827, 10.5194/acp-15-815-2015, 2015.

Gratz, L. E., Keeler, G. J., Marsik, F. J., Barres, J. A., and Dvonch, J. T.: Atmospheric transport of speciated mercury across southern Lake Michigan: Influence from emission sources in the Chicago/Gary urban area, The Science of the total environment, 448, 84-95, 10.1016/j.scitotenv.2012.08.076, 2013.

Hui, M. L., Wu, Q. R., Wang, S. X., Liang, S., Zhang, L., Wang, F. Y., Lenzen, M., Wang, Y. F., Xu, L. X., Lin, Z. T., Yang, H., Lin, Y., Larssen, T., Xu, M., and Hao, J. M.: Mercury Flows in China and Global Drivers, Environmental science & technology, 51, 222-231, 10.1021/acs.est.6b04094, 2017.

Kim, S.-H., Han, Y.-J., Holsen, T. M., and Yi, S.-M.: Characteristics of atmospheric speciated mercury concentrations (TGM, Hg(II) and Hg(p)) in Seoul, Korea, Atmospheric Environment, 43, 3267-3274, 10.1016/j.atmosenv.2009.02.038, 2009.

Landis, M. S., and Keeler, G. J.: Atmospheric mercury deposition to Lake Michigan during the Lake Michigan Mass Balance Study, Environmental science & technology, 36, 4518-4524, 10.1021/es011217b, 2002.

Lee, G.-S., Kim, P.-R., Han, Y.-J., Holsen, T. M., Seo, Y.-S., and Yi, S.-M.: Atmospheric speciated mercury concentrations on an island between China and Korea: sources and transport pathways, Atmospheric Chemistry and Physics, 16, 4119-4133, 10.5194/acp-16-4119-2016, 2016.

Liu, B., Keeler, G. J., Dvonch, J. T., Barres, J. A., Lynam, M. M., Marsik, F. J., and Morgan, J. T.: Urban-rural differences in atmospheric mercury speciation, Atmospheric Environment, 44, 2013-2023, 10.1016/j.atmosenv.2010.02.012, 2010.

Liu, M. D., Chen, L., Wang, X. J., Zhang, W., Tong, Y. D., Ou, L. B., Xie, H., Shen, H. Z., Ye, X. J., Deng, C. Y., and Wang, H. H.: Mercury Export from Mainland China to Adjacent Seas and Its Influence on the Marine Mercury Balance, Environmental science & technology, 50, 6224-6232, 10.1021/acs.est.5b04999, 2016.

Lynam, M. M., and Keeler, G. J.: Automated speciated mercury measurements in Michigan, Environmental science & technology, 39, 9253-9262, 10.1021/es040458r, 2005.

Mao, H., Cheng, I., and Zhang, L.: Current understanding of the driving mechanisms for spatiotemporal variations of atmospheric speciated mercury: a review, Atmos. Chem. Phys., 16, 12897-12924, 10.5194/acp-16-12897-2016, 2016.

Obrist, D., Tas, E., Peleg, M., Matveev, V., Fain, X., Asaf, D., and Luria, M.: Bromine-induced oxidation of mercury in the mid-latitude atmosphere, Nat. Geosci., 4, 22-26, 10.1038/ngeo1018, 2011.

Pacyna, J. M., Travnikov, O., De Simone, F., Hedgecock, I. M., Sundseth, K., Pacyna, E. G., Steenhuisen, F., Pirrone, N., Munthe, J., and Kindbom, K.: Current and future levels of mercury atmospheric pollution on a global scale, Atmos. Chem. Phys., 16, 12495-12511, 10.5194/acp-16-12495-2016, 2016.

Pirrone, N., Cinnirella, S., Feng, X., Finkelman, R. B., Friedli, H. R., Leaner, J., Mason, R., Mukherjee, A. B., Stracher, G. B., Streets, D. G., and Telmer, K.: Global mercury emissions to the atmosphere from anthropogenic and natural sources, Atmos. Chem. Phys., 10, 5951-5964, 10.5194/acp-10-5951-2010, 2010.

Qin, X., Wang, X., Shi, Y., Yu, G., Lin, Y., Fu, Q., Wang, D., Xie, Z., Deng, C., and Huang, K.: Characteristics of atmospheric mercury in East China: implication on sources and formation of mercury species over a regional transport intersection zone, Atmospheric Chemistry and Physics Discussions, 1-36, 10.5194/acp-2018-1164, 2018.

Rutter, A. P., and Schauer, J. J.: The effect of temperature on the gas-particle partitioning of reactive mercury in atmospheric aerosols, Atmospheric Environment, 41, 8647-8657, 10.1016/j.atmosenv.2007.07.024, 2007.

Schroeder, W. H., and Munthe, J.: Atmospheric mercury - An overview, Atmospheric Environment, 32, 809-822, 10.1016/s1352-2310(97)00293-8, 1998.

Streets, D. G., Hao, J. M., Wu, Y., Jiang, J. K., Chan, M., Tian, H. Z., and Feng, X. B.: Anthropogenic mercury emissions in China, Atmospheric Environment, 39, 7789-7806, 10.1016/j.atmosenv.2005.08.029, 2005.

Tang, Y., Wang, S. X., Wu, Q. R., Liu, K. Y., Wang, L., Li, S., Gao, W., Zhang, L., Zheng, H. T., Li, Z. J., and Hao, J. M.: Recent decrease trend of atmospheric mercury concentrations in East China: the influence of anthropogenic emissions, Atmospheric Chemistry and Physics, 18, 8279-8291, 10.5194/acp-18-8279-2018, 2018.

Tian, H. Z., Lu, L., Cheng, K., Hao, J. M., Zhao, D., Wang, Y., Jia, W. X., and Qiu, P. P.: Anthropogenic atmospheric nickel emissions and its distribution characteristics in China, Sci. Total Environ., 417, 148-157, 10.1016/j.scitotenv.2011.11.069, 2012.

van Donkelaar, A., Martin, R. V., Brauer, M., Kahn, R., Levy, R., Verduzco, C., and Villeneuve, P. J.: Global Estimates of Ambient Fine Particulate Matter Concentrations from Satellite-Based Aerosol Optical Depth: Development and Application, Environmental Health Perspectives, 118, 847-855, 10.1289/ehp.0901623, 2010.

Viana, M., Amato, F., Alastuey, A., Querol, X., Moreno, T., Garcia Dos Santos, S., Dolores Herce, M., and Fernandez-Patier, R.: Chemical Tracers of Particulate Emissions from Commercial Shipping, Environmental science & technology, 43, 7472-7477, 10.1021/es901558t, 2009.

Wan, Q., Feng, X., Lu, J., Zheng, W., Song, X., Han, S., and Xu, H.: Atmospheric mercury in Changbai Mountain area, northeastern China I. The seasonal distribution pattern of total gaseous mercury and its potential sources, Environmental Research, 109, 201-206, 10.1016/j.envres.2008.12.001, 2009.

Wang, F., Saiz-Lopez, A., Mahajan, A. S., Martin, J. C. G., Armstrong, D., Lemes, M., Hay, T., and Prados-Roman, C.: Enhanced production of oxidised mercury over the tropical Pacific Ocean: a key missing oxidation pathway, Atmospheric Chemistry and Physics, 14, 1323-1335, 10.5194/acp-14-1323-2014, 2014.

Wang, X., Lin, C.-J., Yuan, W., Sommar, J., Zhu, W., and Feng, X.: Emission-dominated gas exchange of elemental mercury vapor over natural surfaces in China, Atmospheric Chemistry and Physics, 16, 11125-11143, 10.5194/acp-16-11125-2016, 2016.

Wang, Y. Q., Zhang, X. Y., and Draxler, R. R.: TrajStat: GIS-based software that uses various trajectory statistical analysis methods to identify potential sources from long-term air pollution measurement data, Environmental Modelling & Software, 24, 938-939, 10.1016/j.envsoft.2009.01.004, 2009.

Wright, L. P., Zhang, L., and Marsik, F. J.: Overview of mercury dry deposition, litterfall, and throughfall studies, Atmos. Chem. Phys., 16, 13399-13416, 10.5194/acp-16-13399-2016, 2016.

Wright, L. P., Zhang, L. M., Cheng, I., Aherne, J., and Wentworth, G. R.: Impacts and Effects Indicators of Atmospheric Deposition of Major Pollutants to Various Ecosystems - A Review, Aerosol Air Qual. Res., 18, 1953-1992, 10.4209/aaqr.2018.03.0107, 2018.

Wu, Q. R., Wang, S. X., Li, G. L., Liang, S., Lin, C. J., Wang, Y. F., Cai, S. Y., Liu, K. Y., and Hao, J. M.: Temporal Trend and Spatial Distribution of Speciated Atmospheric Mercury Emissions in China During 1978-2014, Environmental science & technology, 50, 13428-13435, 10.1021/acs.est.6b04308, 2016.

Xu, L. L., Chen, J. S., Yang, L. M., Niu, Z. C., Tong, L., Yin, L. Q., and Chen, Y. T.: Characteristics and sources of atmospheric mercury speciation in a coastal city, Xiamen, China, Chemosphere, 119, 530-539, 10.1016/j.chemosphere.2014.07.024, 2015.

Xu, X., Liao, Y., Cheng, I., and Zhang, L.: Potential sources and processes affecting speciated atmospheric mercury at Kejimkujik National Park, Canada: comparison of receptor models and data treatment methods, Atmospheric Chemistry and Physics, 17, 1381-1400, 10.5194/acp-17-1381-2017, 2017.

Ye, Z., Mao, H., Lin, C. J., and Kim, S. Y.: Investigation of processes controlling summertime gaseous elemental mercury oxidation at midlatitudinal marine, coastal, and inland sites, Atmos. Chem. Phys., 16, 8461-8478, 10.5194/acp-16-8461-2016, 2016.

Zhang, L., Wang, S. X., Wang, L., and Hao, J. M.: Atmospheric mercury concentration and chemical speciation at a rural site in Beijing, China: implications of mercury emission sources, Atmospheric Chemistry and Physics, 13, 10505-10516, 10.5194/acp-13-10505-2013, 2013.

Zhang, L., Wang, S. X., Wang, L., Wu, Y., Duan, L., Wu, Q. R., Wang, F. Y., Yang, M., Yang, H., Hao, J. M., and Liu, X.: Updated Emission Inventories for Speciated Atmospheric Mercury from

735   Anthropogenic Sources in China, Environmental science & technology, 49, 3185-3194,
736   10.1021/es504840m, 2015.

737 Zhang, L., Lyman, S., Mao, H., Lin, C.-J., Gay, D. A., Wang, S., Gustin, M. S., Feng, X., and Wania, F.:
738   A synthesis of research needs for improving the understanding of atmospheric mercury cycling,
739   Atmospheric Chemistry and Physics, 17, 9133-9144, 10.5194/acp-17-9133-2017, 2017.

740 Zhu, J., Wang, T., Talbot, R., Mao, H., Hall, C. B., Yang, X., Fu, C., Zhuang, B., Li, S., Han, Y., and
741   Huang, X.: Characteristics of atmospheric Total Gaseous Mercury (TGM) observed in urban
742   Nanjing, China, Atmospheric Chemistry and Physics, 12, 12103-12118, 10.5194/acp-12-12103-
743   2012, 2012.

744 Zhu, J., Wang, T., Bieser, J., and Matthias, V.: Source attribution and process analysis for atmospheric
745   mercury in eastern China simulated by CMAQ-Hg, Atmospheric Chemistry and Physics, 15, 8767-
746   8779, 10.5194/acp-15-8767-2015, 2015.

747 Zhu, W., Lin, C.-J., Wang, X., Sommar, J., Fu, X., and Feng, X.: Global observations and modeling of
748   atmosphere–surface exchange of elemental mercury: a critical review, Atmospheric Chemistry and
749   Physics, 16, 4451-4480, 10.5194/acp-16-4451-2016, 2016.

750

751
752
753
754
755
756
757
758
759
760
761
762
763
764
765
766
767
768
769
770
771
772
773
774
775
776
777
778

779
780
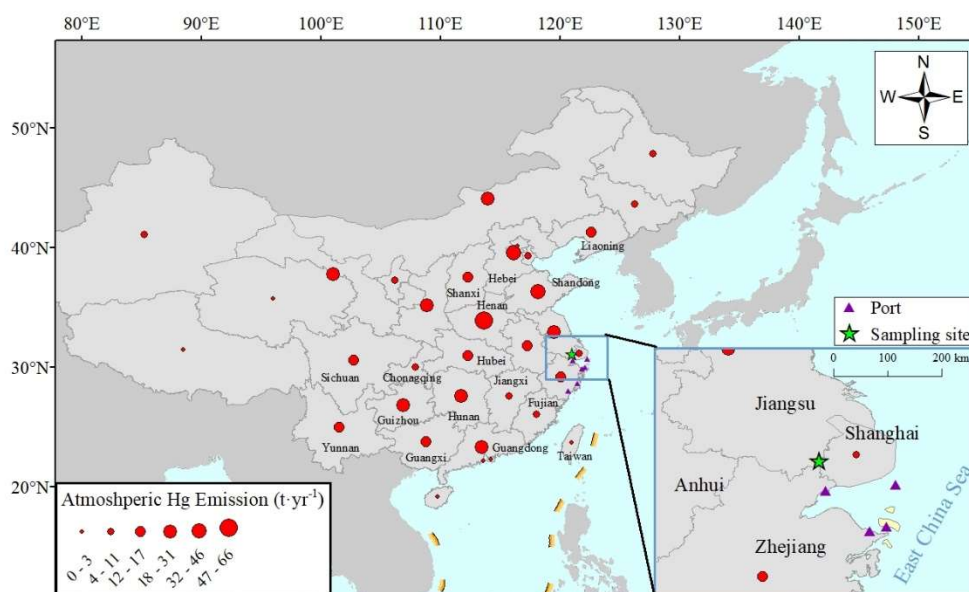
781
782
Figure 1. The location of the Dianshan Lake (DSL) site in Shanghai, China. The red dots in the map represent the anthropogenic atmospheric Hg emissions by each province in 2014 (Wu et al., 2016).
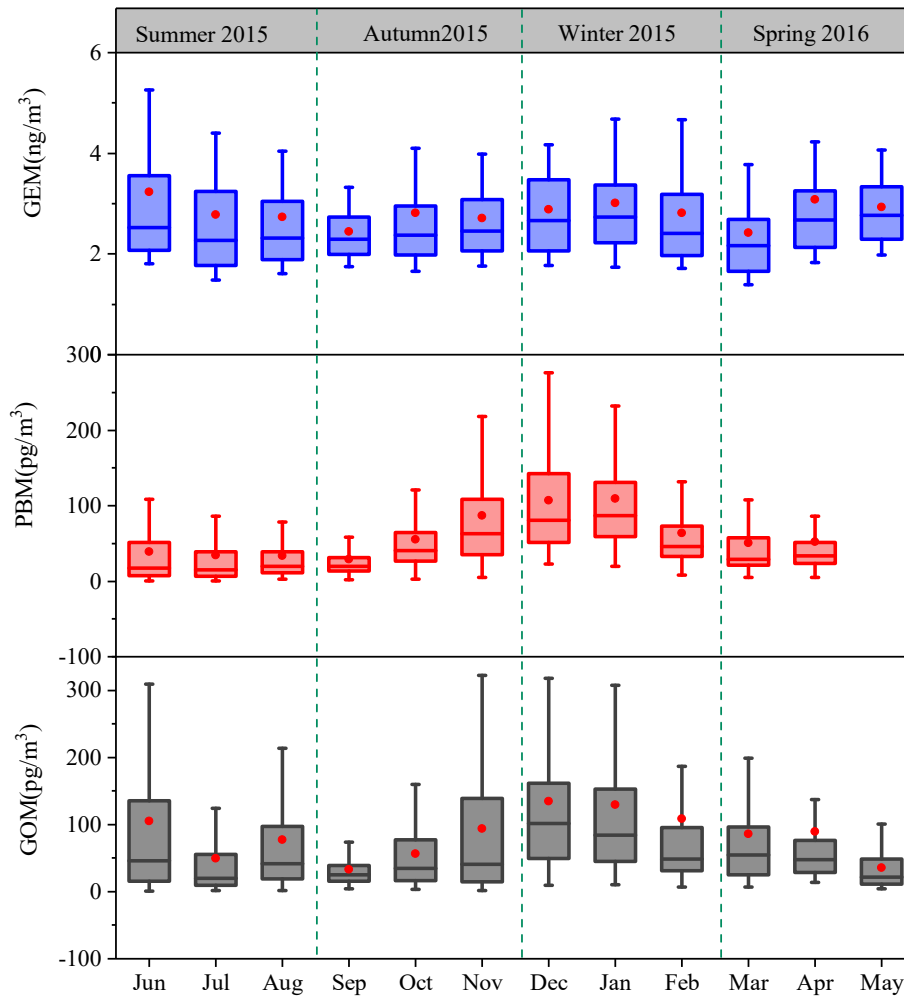
786

787
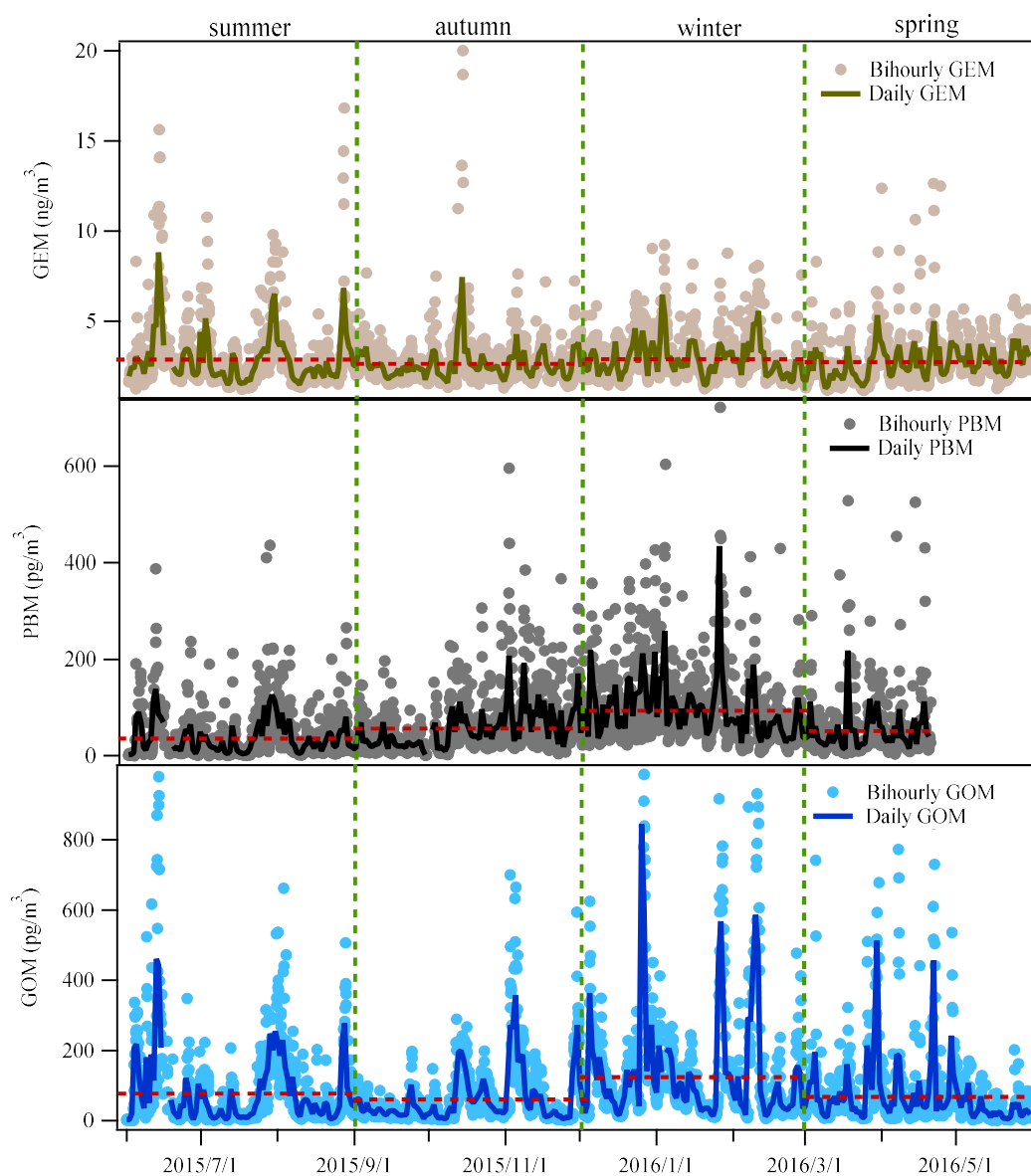
788
789 Figure 2. Time series of atmospheric Hg (GEM, PBM and GOM) concentrations during the whole
790 study period at DSL. The red-dashed lines represent the mean concentrations of Hg species in
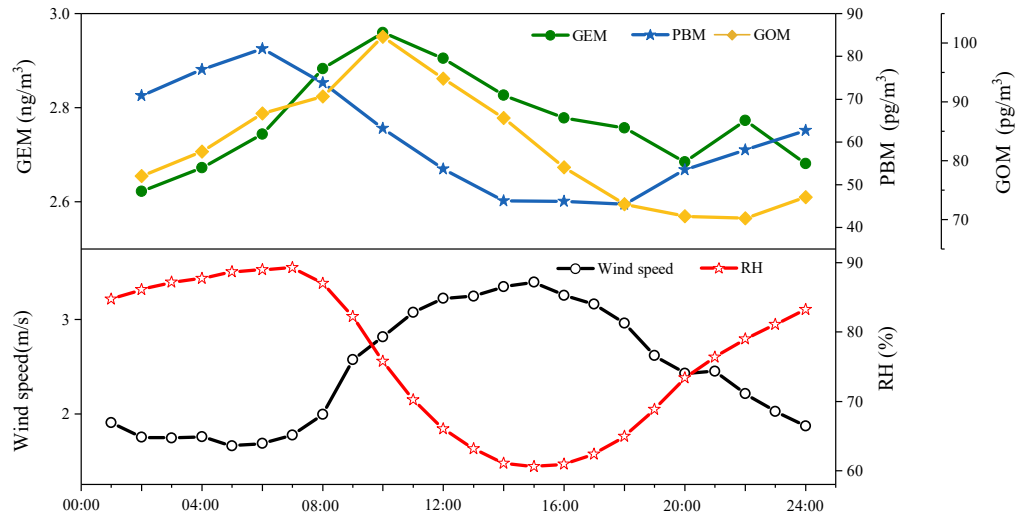791 each season.
792
793
794
795

796

Figure 3. Monthly variation of GEM, PBM, and GOM concentrations. The 10th，25th, median, 75th
and 90th percentile values are indicated in the box plots. The red dots represent the mean values.

799

800
801
802   Figure 4. Annual mean diurnal variation of GEM, PBM, and GOM concentrations.
803
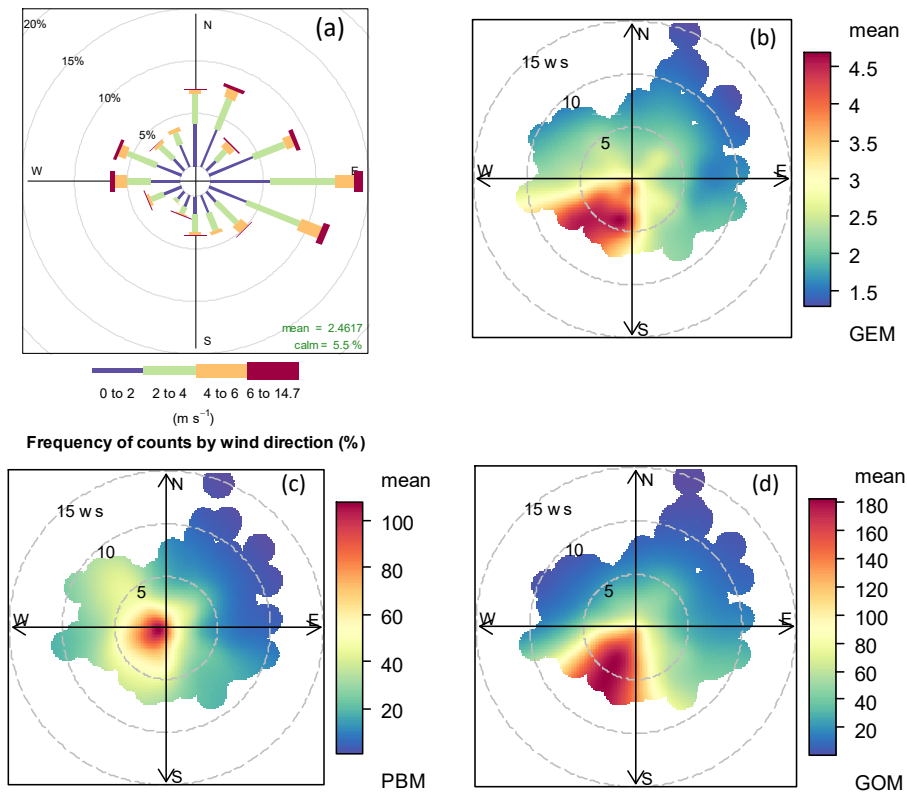
804
805

806   Figure 5. (a) Wind rose plot during the study period. Mean concentrations of (b) GEM, (c) PBM,

807   and (d) GOM as a function of wind speed and wind directions. The radii of the circle in Figure 5 (a)

808   represent the frequency of wind directions and the radii of the circle in Figure 5 (b), (c), and (d)

809   represent the value of wind speed.
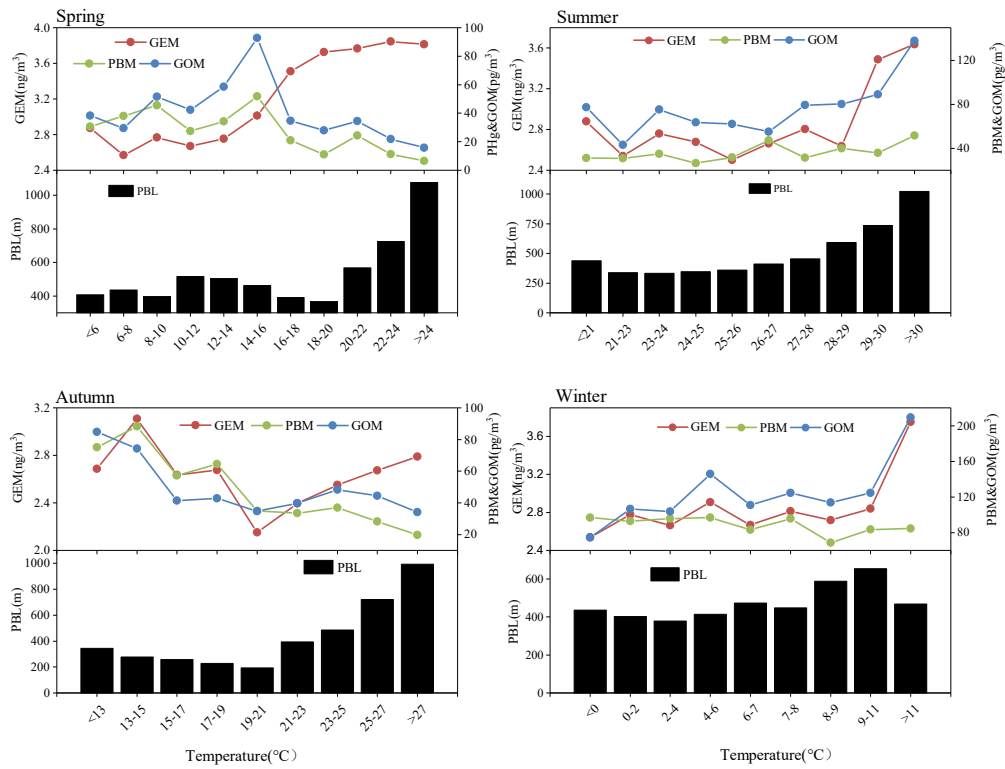
810

811   Figure 6. The variation of atmospheric Hg (GEM, PBM, and GOM) and PBL as a function of

812   temperature in all four seasons.

813
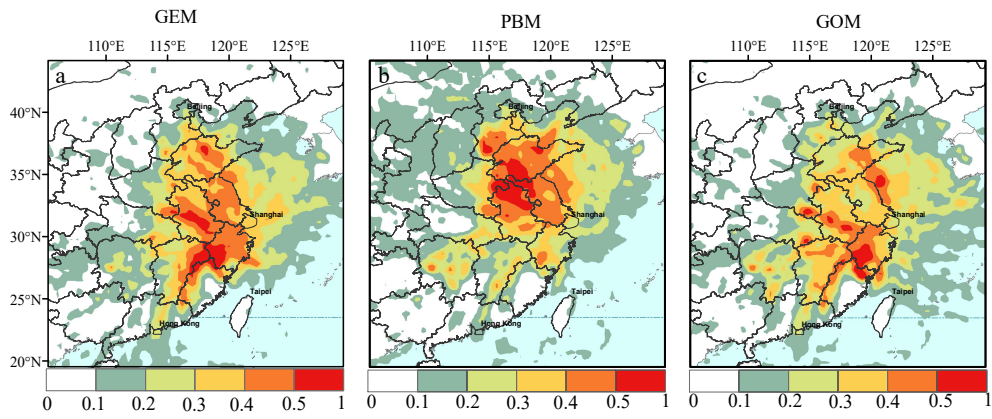
Figure 7. Potential source regions of atmospheric Hg (GEM, PBM, and GOM) at the observational site according to PSCF analysis.
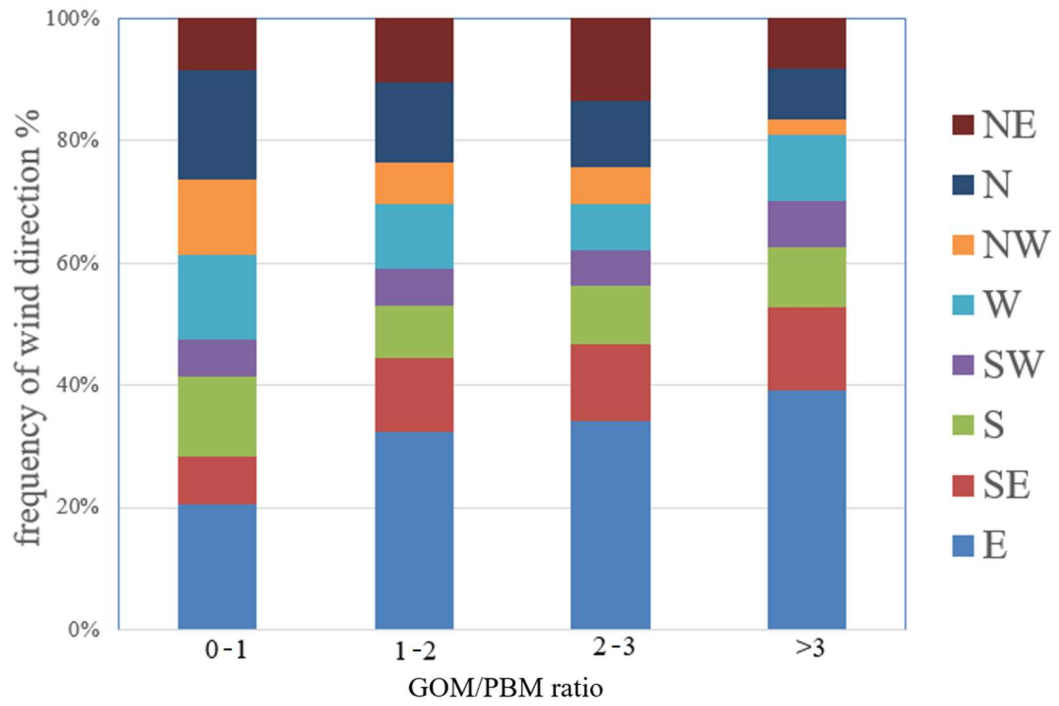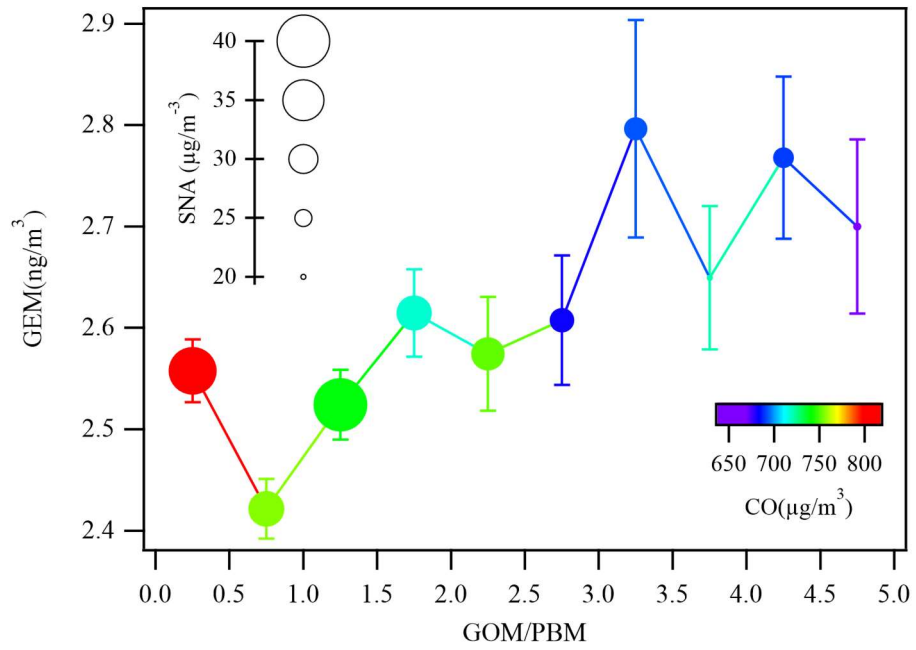
818

819 Figure 8. Frequency of wind directions under different ranges of GOM/PBM ratios.

820

821

Figure 9. The GEM concentrations as a function of the GOM/PBM ratios in each bin of 0.5. The dots are colored by the concentrations of CO and the sizes of the dots represent the concentrations of SNA in $PM_{2.5}$. The bars represent one standard error of GEM concentration in each bin.
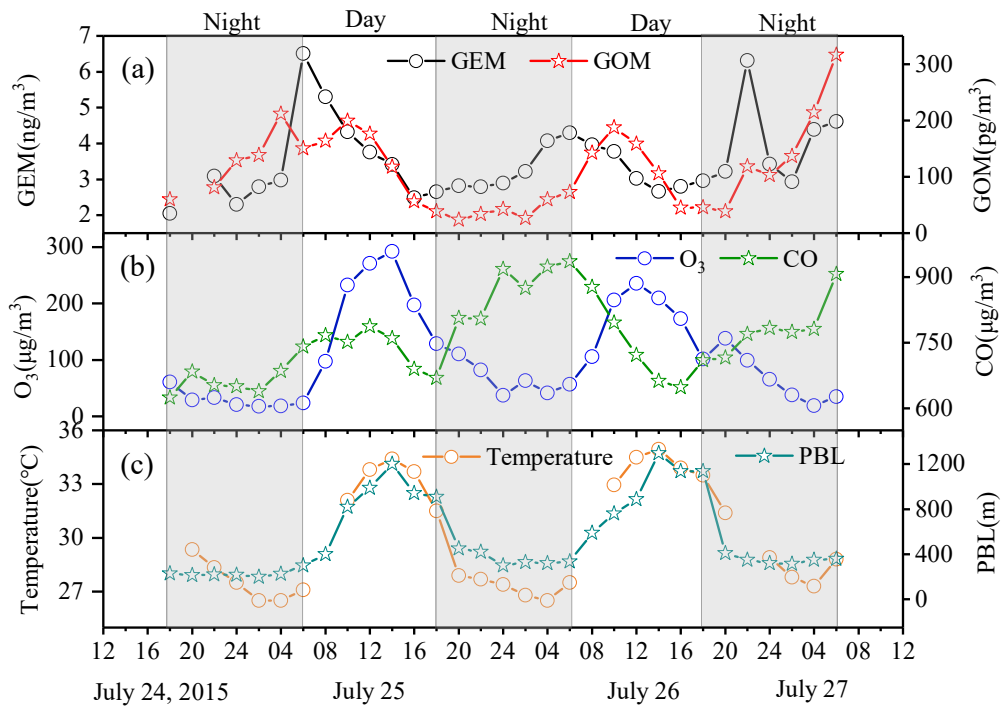
825

826
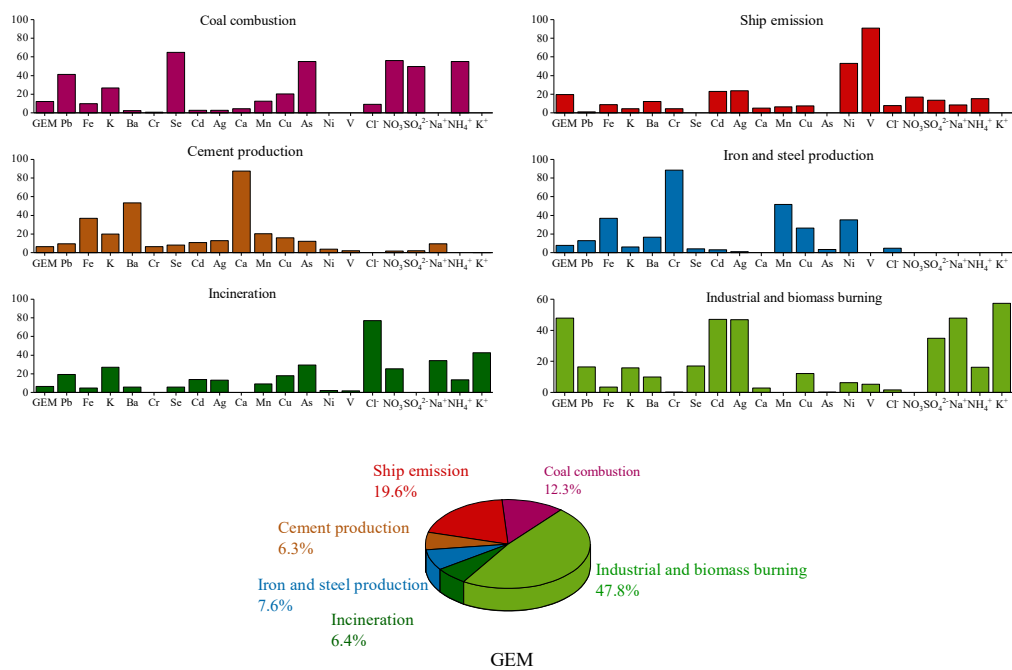
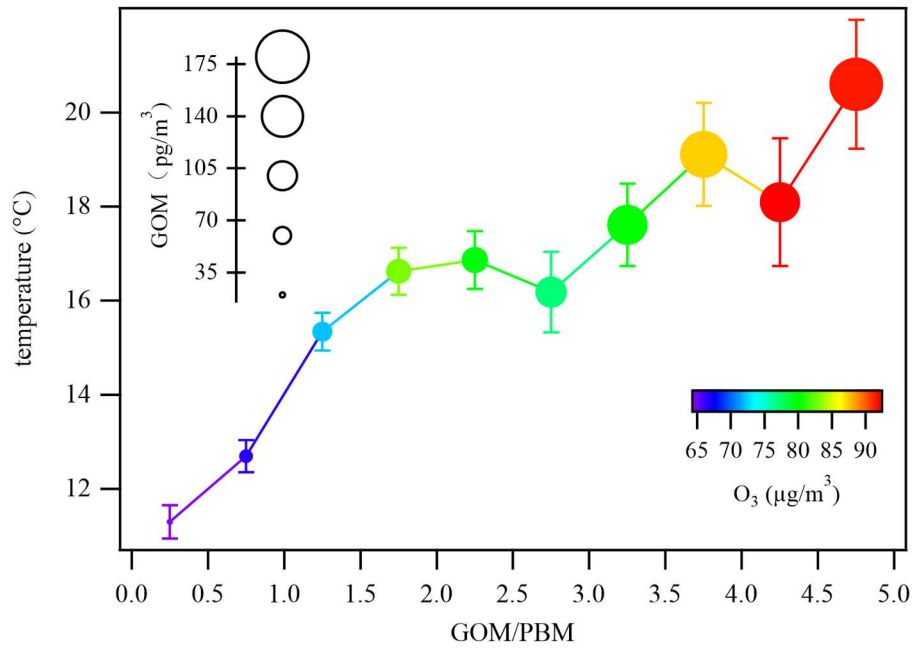Figure 10. A six factor source apportionment for anthropogenic GEM based on PMF analysis.

828

829

830 Figure 11. A case study of GEM oxidation from July 24 to 27, 2015. The time-series of GEM, GOM,

831 O_3, CO, temperature, and PBL are plotted. The shaded parts represent nighttime.
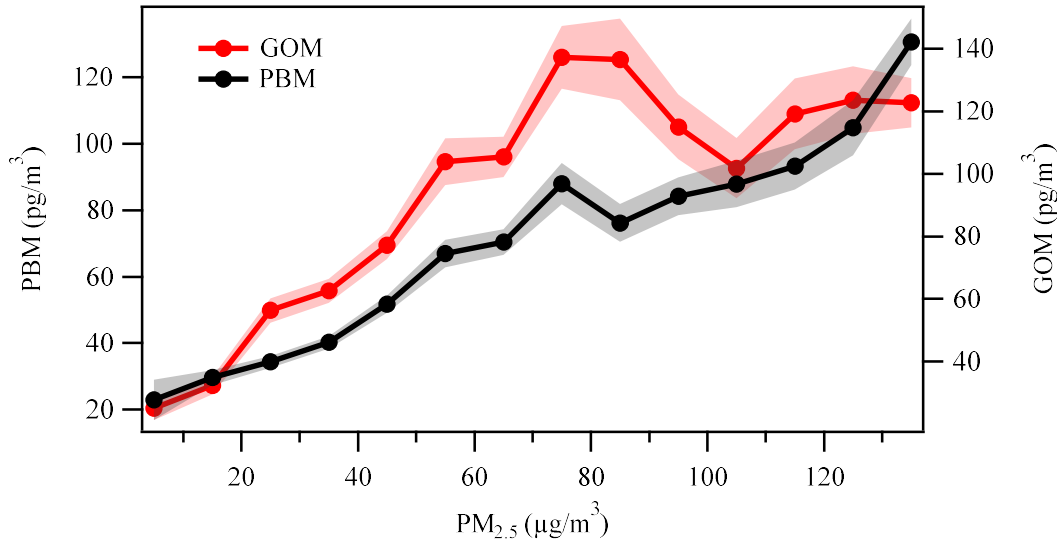
832

833

834   Figure 12. Temperature variations in each bin of the GOM/PBM ratios. The dots are colored by the

835   concentrations of O_3 and the sizes of the dots represent the concentrations of GOM. The bars

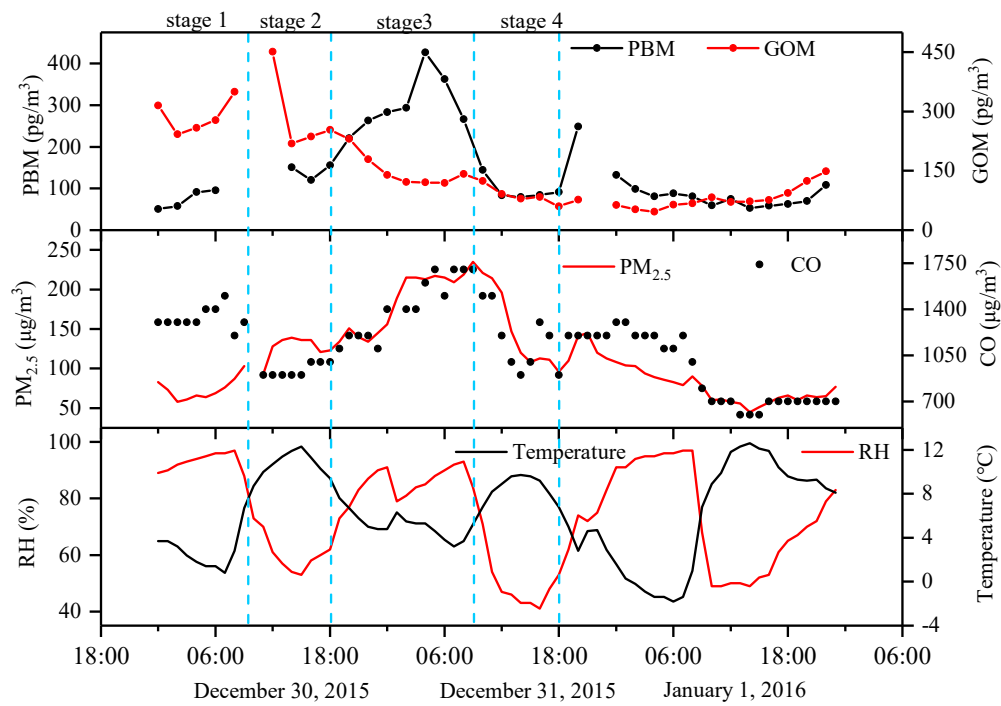836   represent one standard error of temperature in each bin.

837

838

839

Figure 13. The variations of PBM and GOM as a function of $PM_{2.5}$ in each bin of 10 μg/m³. The
shaded areas represent one standard error of GOM and PBM concentrations.

842

843

844 Figure 14. A case study of gas-particle portioning between GOM and PBM from December 30, 2015

845 to January 1, 2016, which was divided into different stages. The time-series of PBM, GOM, $PM_{2.5}$,

846 CO, temperature, and RH are plotted.

Table 1. The concentrations of speciated atmospheric mercury in this study and other sites around the world.

Location	Remarks	Year	GEM (ng/m^3)	PHg (pg/m^3)	RGM (pg/m^3)	Reference
Dianshan Lake Shanghai, China	Suburban	2015-2016	2.77±1.36	60.8±67.4	82.13±115.5	This study
Chongming Shanghai, China	Suburban	2009-2012	2.65±1.73	21.5±25.4	8.0±8.8	Zhang et al. (2017)
Xiamen, China	Suburban	2012-2013	3.5	174.41	61.05	Xu et al. (2015)
Guiyang, China	Urban	2009	9.72±10.2	368±676	35.7±43.9	Fu et al. (2011)
Miyun, China	Rural	2008-2009	3.23	98.2	10.1	Zhang et al. (2013)
Mt.Waliguan, China	Remote	2007-2008	1.98±0.98	19.4±18.1	7.4±4.8	Wan et al. (2009)
Seoul, Korea	Urban	2005-2006	3.22±2.10	23.9±19.6	27.2±19.3	Kim et al. (2009)
Nova Scotia, Canada	Rural	2010-2011	1.38±0.2	0.4±1.0	3.5±4.5	Cheng et al. (2014)
Elora,Ontario, Canada	Rural	2006-2007	1.17	16.40	15.1	Baya and Van Heyst (2010)
Chicago, USA	Urban	2007	2.5±1.5	9±20	17±87	Gratz et al. (2013)
Reno,USA	Suburban	2007-2009	2.0±0.7	7±7	18±22	Lyman and Gustin (2009)
Rochester, NY, USA	Urban	2008-2009	1.49	6.57	4.08	Huang et al. (2010)

Table 2. PCA (Principal Component Analysis) analysis for GEM at DSL.

	Factor 1	Factor 2	Factor 3	Factor 4
GEM	0.50	0.25	0.11	0.07
SO_2	**0.69**	-0.20	-0.18	0.35
NO_2	0.38	-0.49	0.35	0.39
SO_4^{2-}	**0.84**	0.13	0.15	0.00
NH_4^+	**0.88**	-0.12	0.18	0.07
K^+	**0.77**	-0.25	0.04	0.39
Pb	**0.80**	-0.17	0.04	0.32
Se	**0.87**	-0.05	0.01	0.29
As	**0.82**	-0.23	0.06	0.33
O_3	0.06	**0.79**	-0.30	0.03
NH_3	0.03	**0.73**	0.36	-0.04
Temperature	-0.23	**0.82**	0.17	-0.03
Ni	0.24	-0.02	**0.85**	0.22
V	-0.03	0.11	**0.90**	-0.05
Fe	0.50	-0.12	0.24	**0.74**
Ca	0.26	0.08	0.00	**0.90**
Explained variance %	34.15	14.85	13.43	12.89